# The impact of film deposition and annealing on the nanostructure and charge mobility in the photoactive layer of organic homojunction solar cells

Lachlan Packman, Neil Mallo, Aaron Raynor, Mile Gao, Mohammad Babazadeh, Hui Jin, David M. Huang,[†] Paul L. Burn,* and Ian R. Gentle,* Paul E. Shaw

Centre for Organic Photonics & Electronics (COPE), School of Chemistry and Molecular Biosciences, The University of Queensland, Brisbane, QLD 4072, Australia

†Department of Chemistry, School of Physics, Chemistry and Earth Sciences, The University of Adelaide, Adelaide South Australia, 5005, Australia
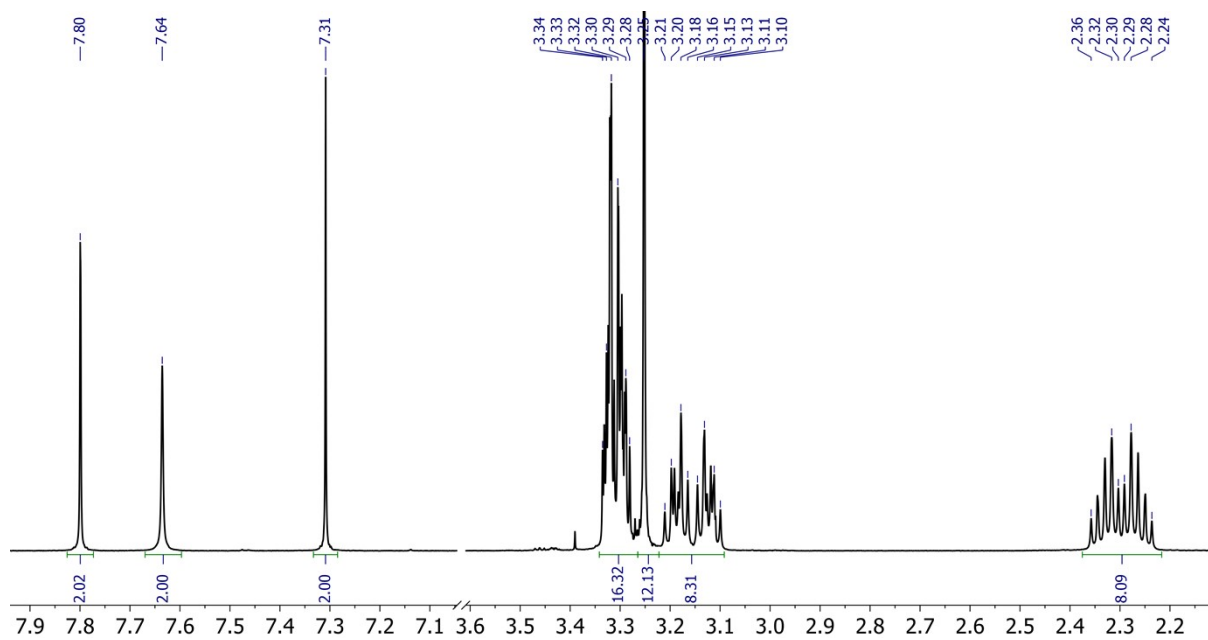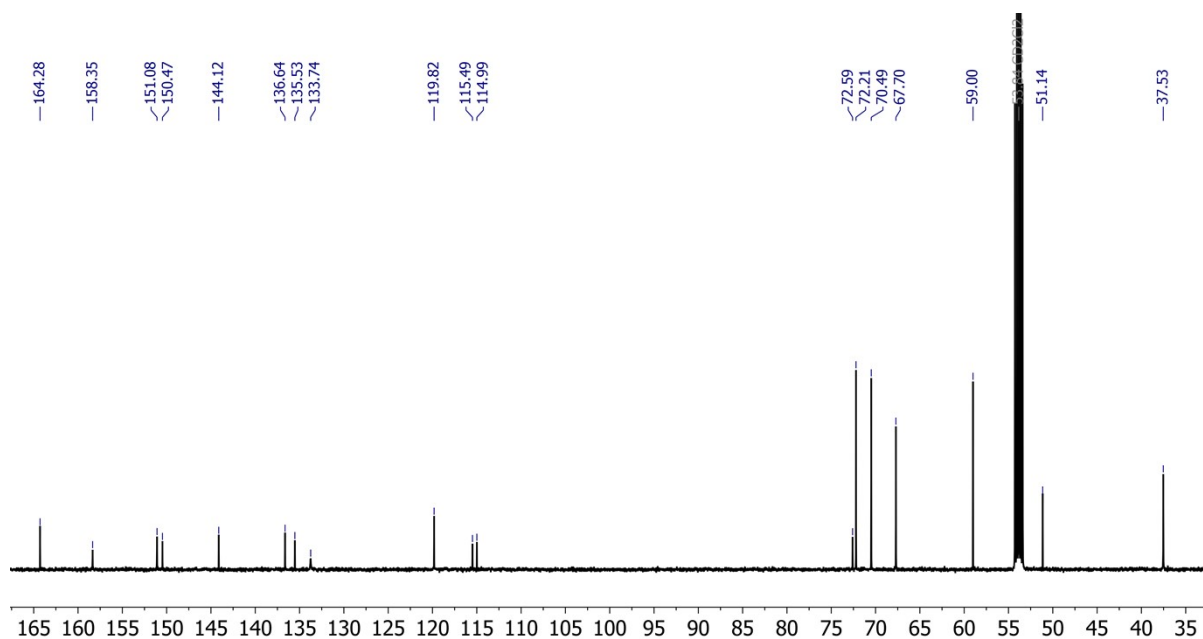
*Email: p.burn2@uq.edu.au; i.gentle@uq.edu.au
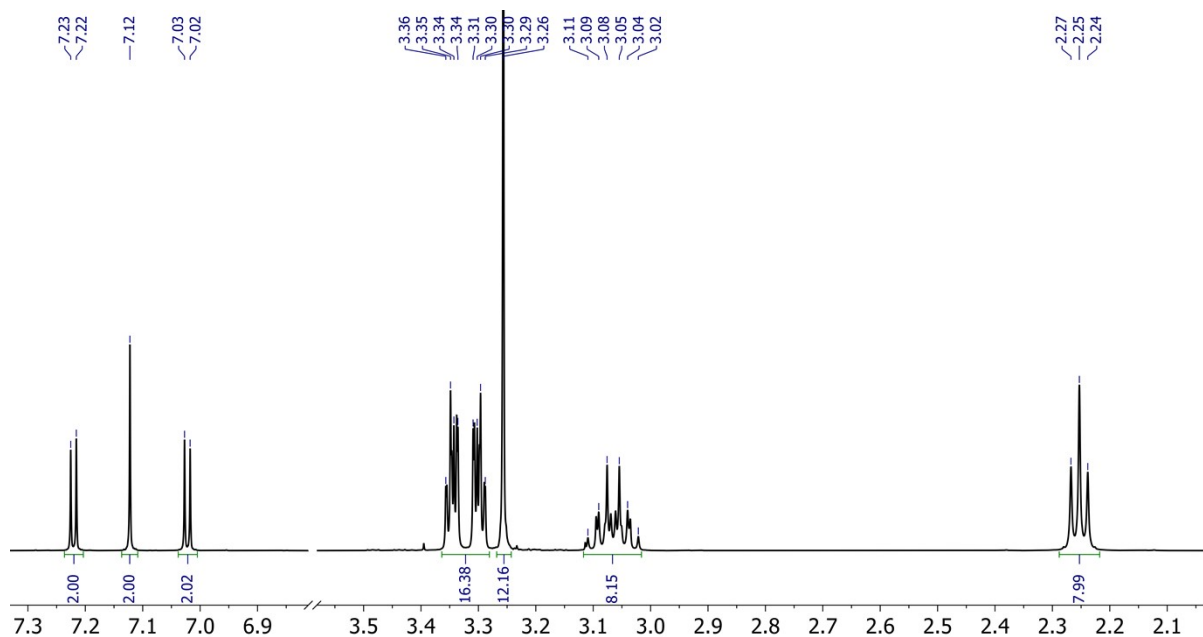
Figure S1. ^{1}H NMR (500 MHz, CD_2Cl_2, 298 K) spectrum of **2**.
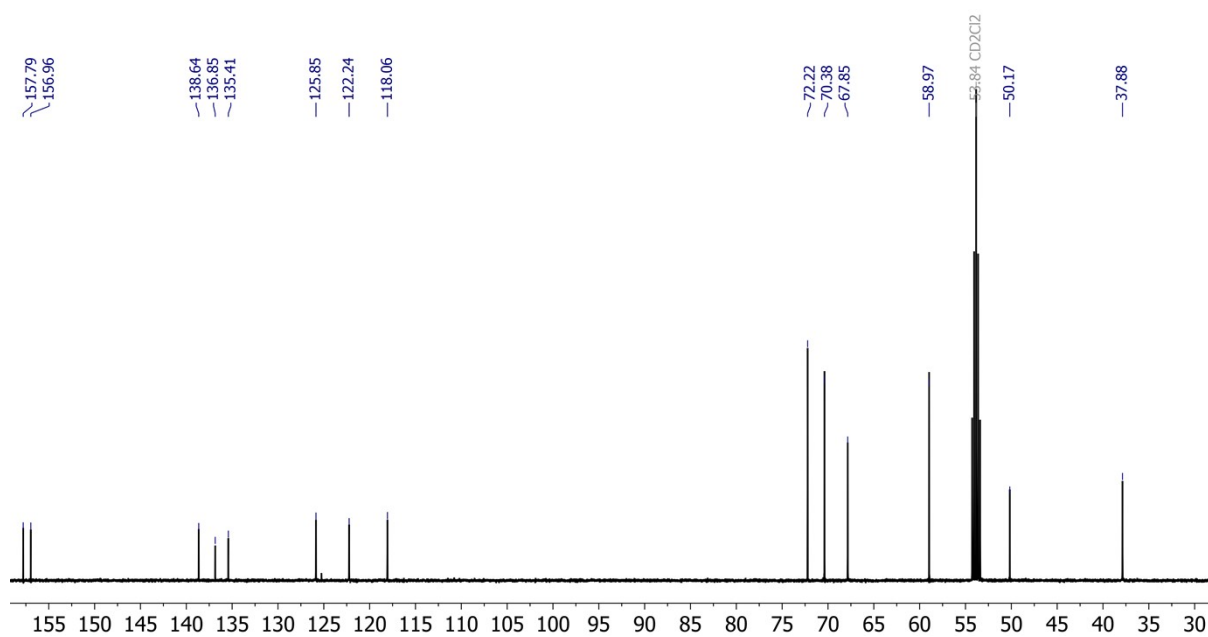
Figure S2. $^{13}C\{^1H\}$ NMR (126 MHz, CD_2Cl_2, 298 K) spectrum of **2**.

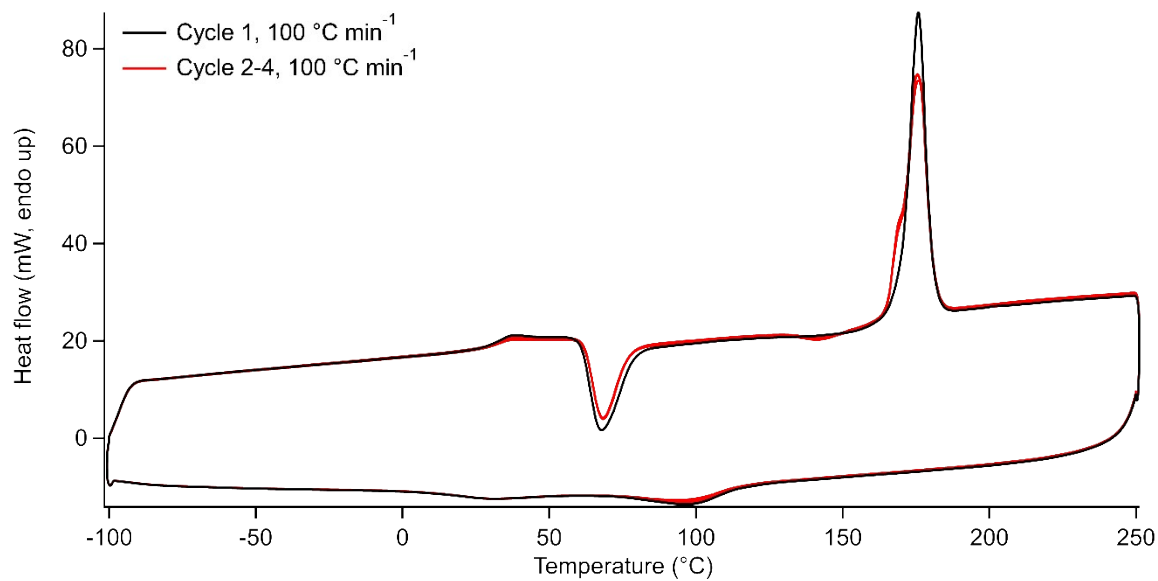**Figure S3**. ^1H NMR (500 MHz, CD_2Cl_2, 298 K) spectrum of **D(CPDT-DCV)**.

Figure S4. $^{13}C\{^1H\}$ NMR (126 MHz, CD_2Cl_2, 298 K) spectrum of **D(CPDT-DCV)**.
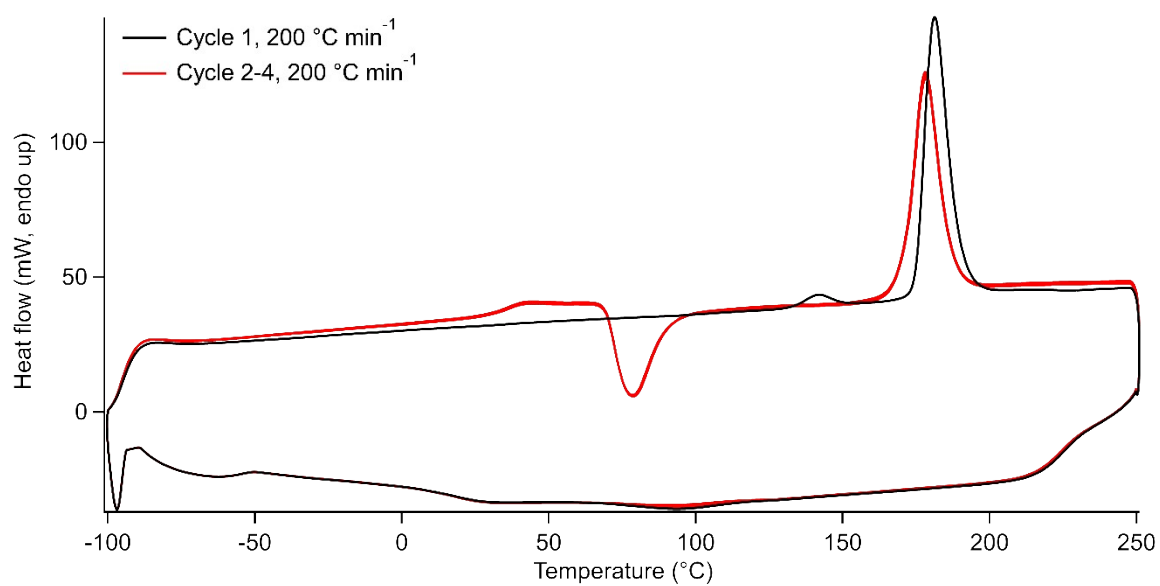
**Figure S5**. The DSC thermogram of **D(CPDT-DCV)**, measured at a scan rate 200 °C min^{-1}. The first heating/cooling cycle is plotted in black, subsequent cycles are plotted in red.

Figure S6. The DSC thermogram of **D(CPDT-DCV)**, measured at a scan rate 100 °C min^{-1}. The first heating/cooling cycle is plotted in black, subsequent cycles are plotted in red.
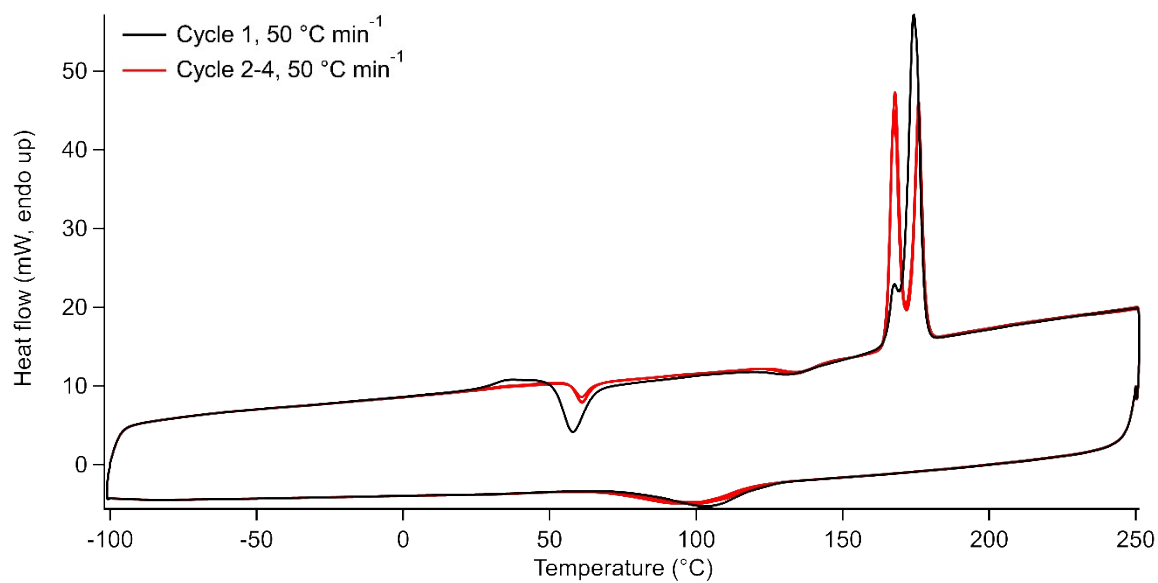
Figure S7. The DSC thermogram of **D(CPDT-DCV)**, measured at a scan rate 50 °C min^{-1}. The first heating/cooling cycle is plotted in black, subsequent cycles are plotted in red.
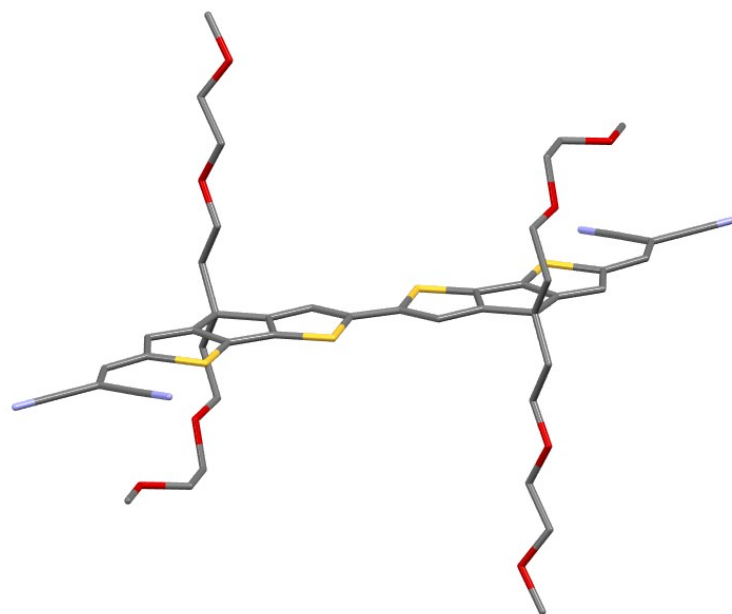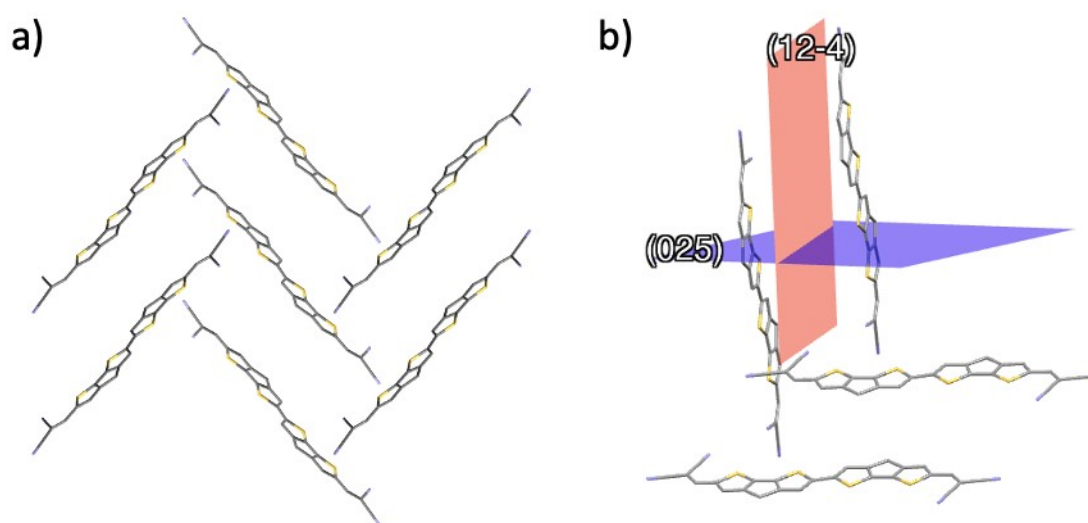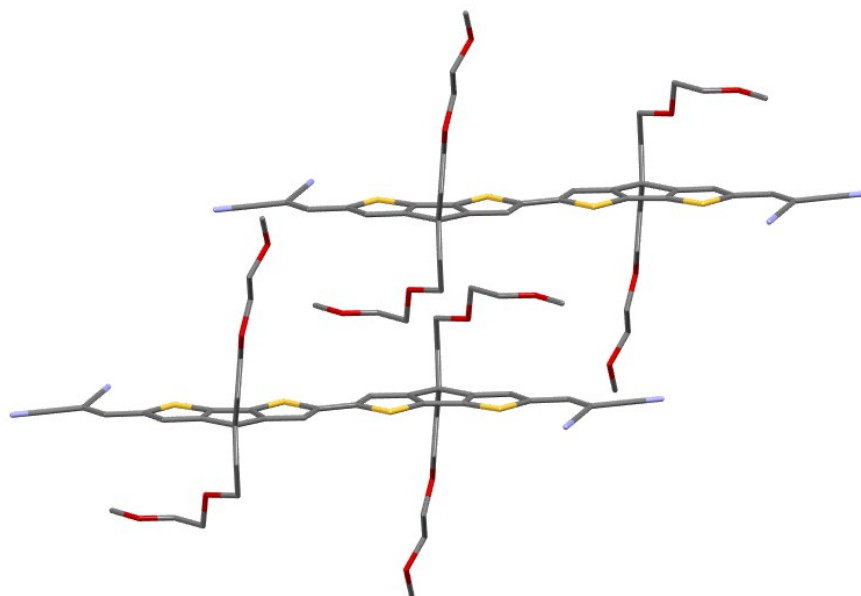
Figure S8. Single crystal structure of a **D(CPDT-DCV)** molecule. H atoms have been omitted for clarity.


Figure S9. a) Herringbone packing motif of the **D(CPDT-DCV)** single crystal structure. b) Shows the (12-4) and (025) hkl planes for this crystal structure. H atoms and glycolated side chains have been omitted for clarity.

Figure S10. Intercalation of the glycolated side chains between the aromatic planes of the **D(CPDT-DCV)** molecules within the **D(CPDT-DCV)** single crystal structure. H atoms have been omitted for clarity.

Data were collected using an Oxford Rigaku Synergy-S employing confocal mirror monochromated Mo-K$_\alpha$ radiation generated from a microfocus source (0.71073 Å) with ω and ψ scans at 100(2) K.[1] Data integration and reduction were undertaken with CrysAlisPro.[1] Subsequent computations were carried out using Olex2.[2] Structures were solved with ShelXT and refined and extended with ShelXL.[3,4] Carbon-bound hydrogen atoms were included in idealised positions and refined using a riding model.

Crystal Data for $C_{46}H_{50}N_4O_8S_4$ (M = 915.14 g/mol): monoclinic, space group P2$_1$/c (no. 14), a = 9.2402(4) Å, b = 10.7034(5) Å, c = 22.9820(12) Å, β = 97.437(4)°, V = 2253.83(19) Å^3, Z = 2, T = 100(2) K, μ(Mo Kα) = 0.269 mm^{-1}, D_{calc} = 1.348 g/cm^3, 29935 reflections measured (5.222° ≤ 2Θ ≤ 56.558°), 5606 unique (R_{int} = 0.0827, R$_{sigma}$ = 0.0521) which were used in all calculations. The final R_1 was 0.0613 (I > 2σ(I)) and wR_2 was 0.1574 (all data).
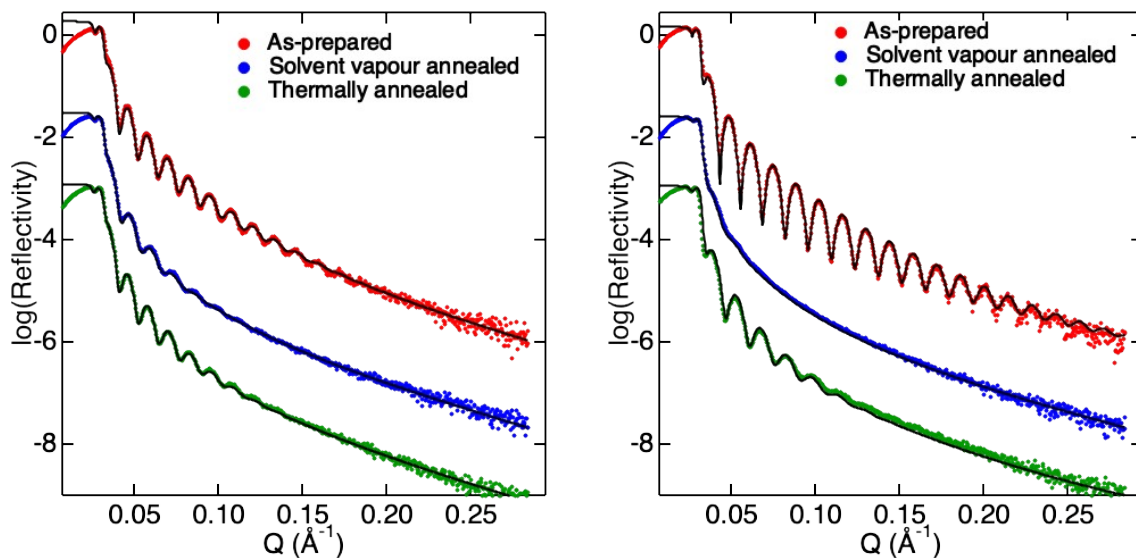
Figure S11. X-ray reflectivity profiles of solution processed (left) and thermally deposited (right) **D(CPDT-DCV)** films used to calculate the density of the films. All films had a density of 1.3 g cm^{-3}.
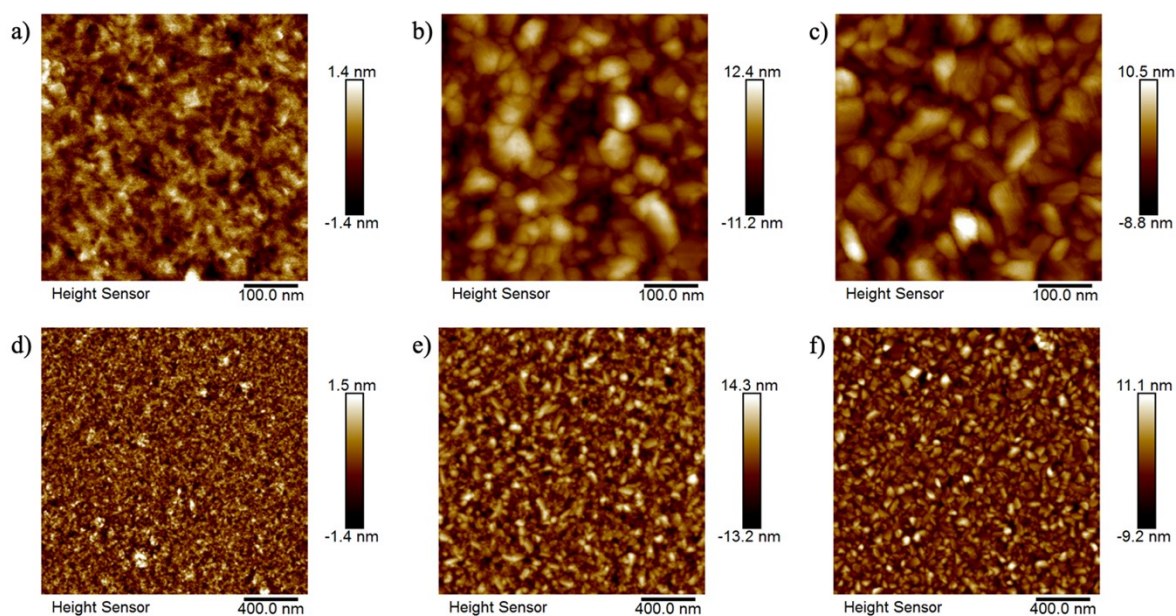
Figure S12: Atomic force microscopy (AFM) topographical images of thermally deposited **D(CPDT-DCV)** films. The top graphs (a-c) are at higher magnification than bottom images (d-f). (a, d) as-prepared, (b, e) solvent vapour annealed, and (c, f) was thermally annealed.
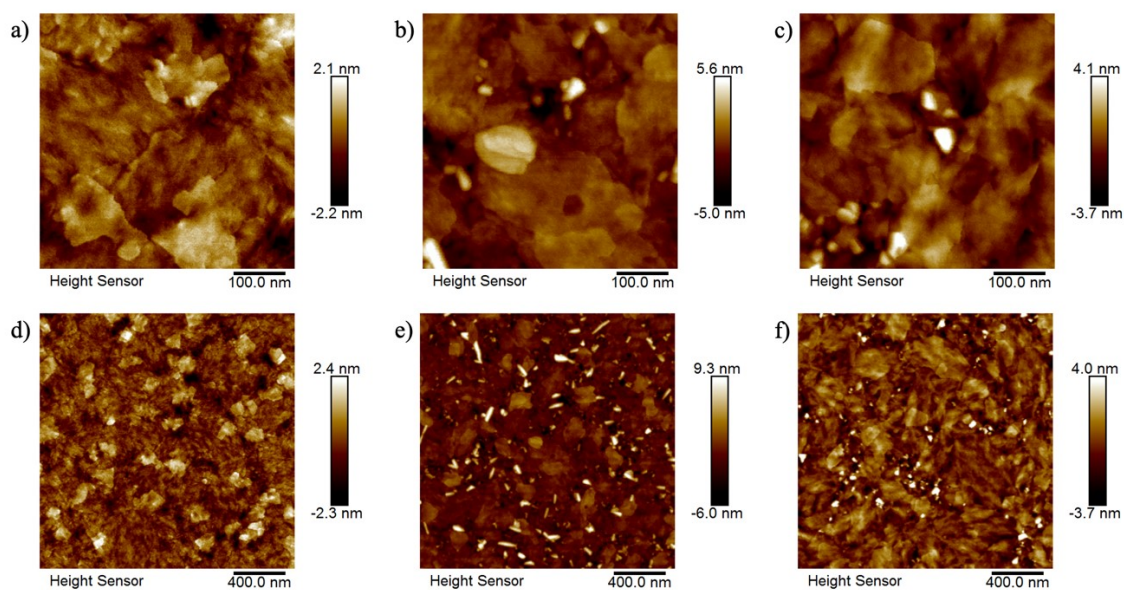
Figure S13: Atomic force microscopy (AFM) topographical images of solution processed **D(CPDT-DCV)** films. The top graphs (a-c) are at higher magnification than bottom images (d-f). (a, d) as-prepared, (b, e) solvent vapour annealed, (c, f) was thermally annealed.

Table S1. Energy, E, wavelength, λ, and oscillator strength, f, from TD-DFT calculations of 3 lowest energy singlet absorption transitions of **D(CPDT-DCV)**.
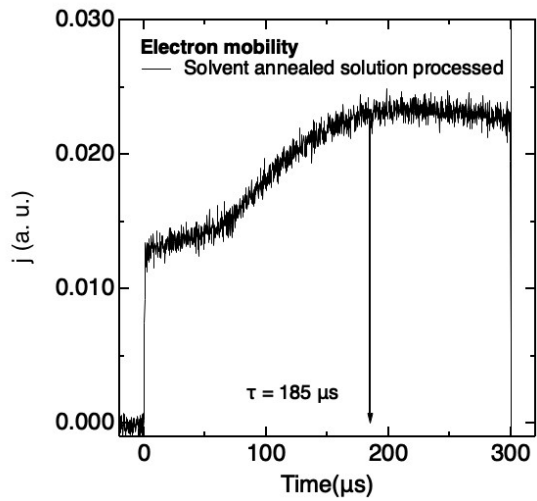
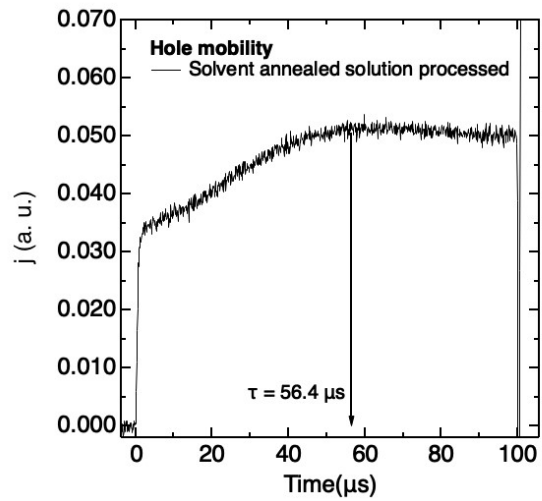| Transition	E (eV)	λ (nm)	f
1	2.25	551	2.500
2	2.97	417	0.000
3	3.90	318	0.256
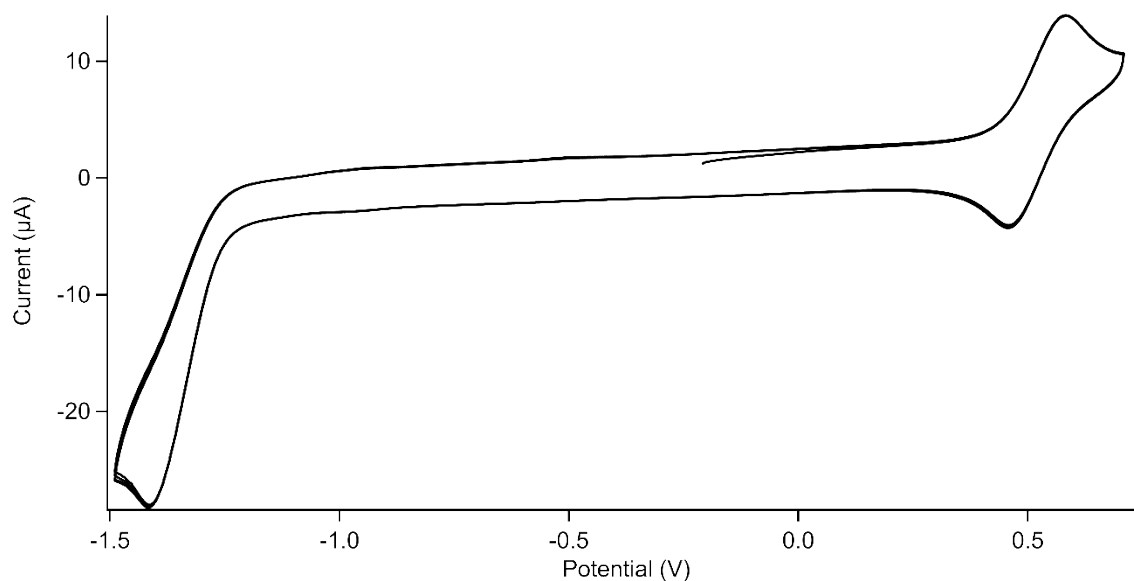
Figure S14. Cyclic voltammogram (4 cycles) of **D(CPDT-DCV)**, recorded in 0.1M TBAP in DCM. The data were collected with a scan rate of 50 mV s⁻¹, and are referenced against Fc/Fc⁺.
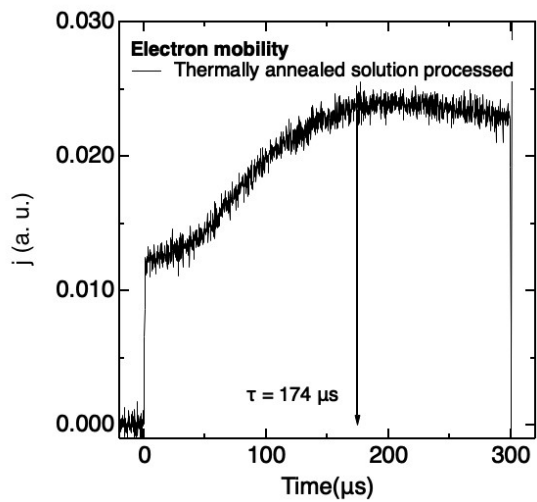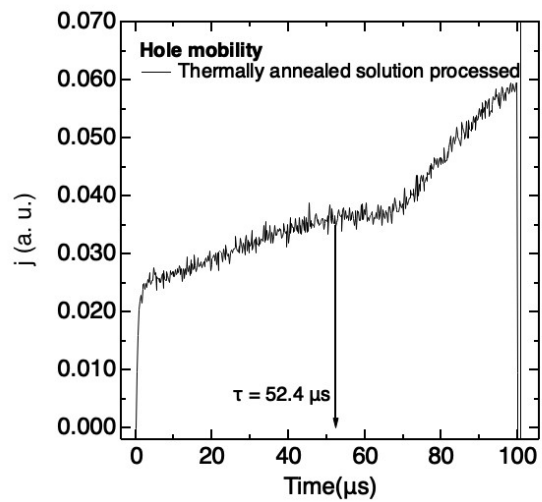
a)   b)
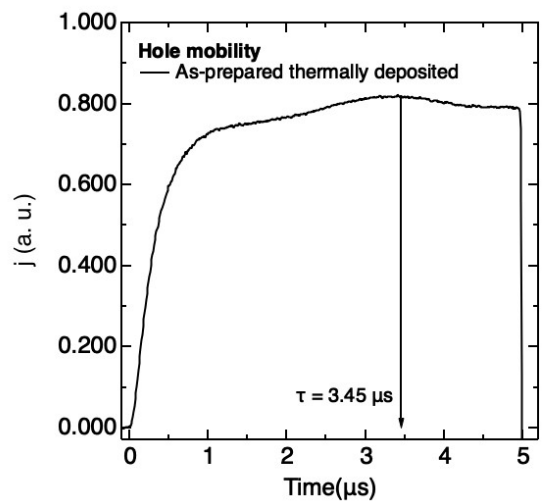
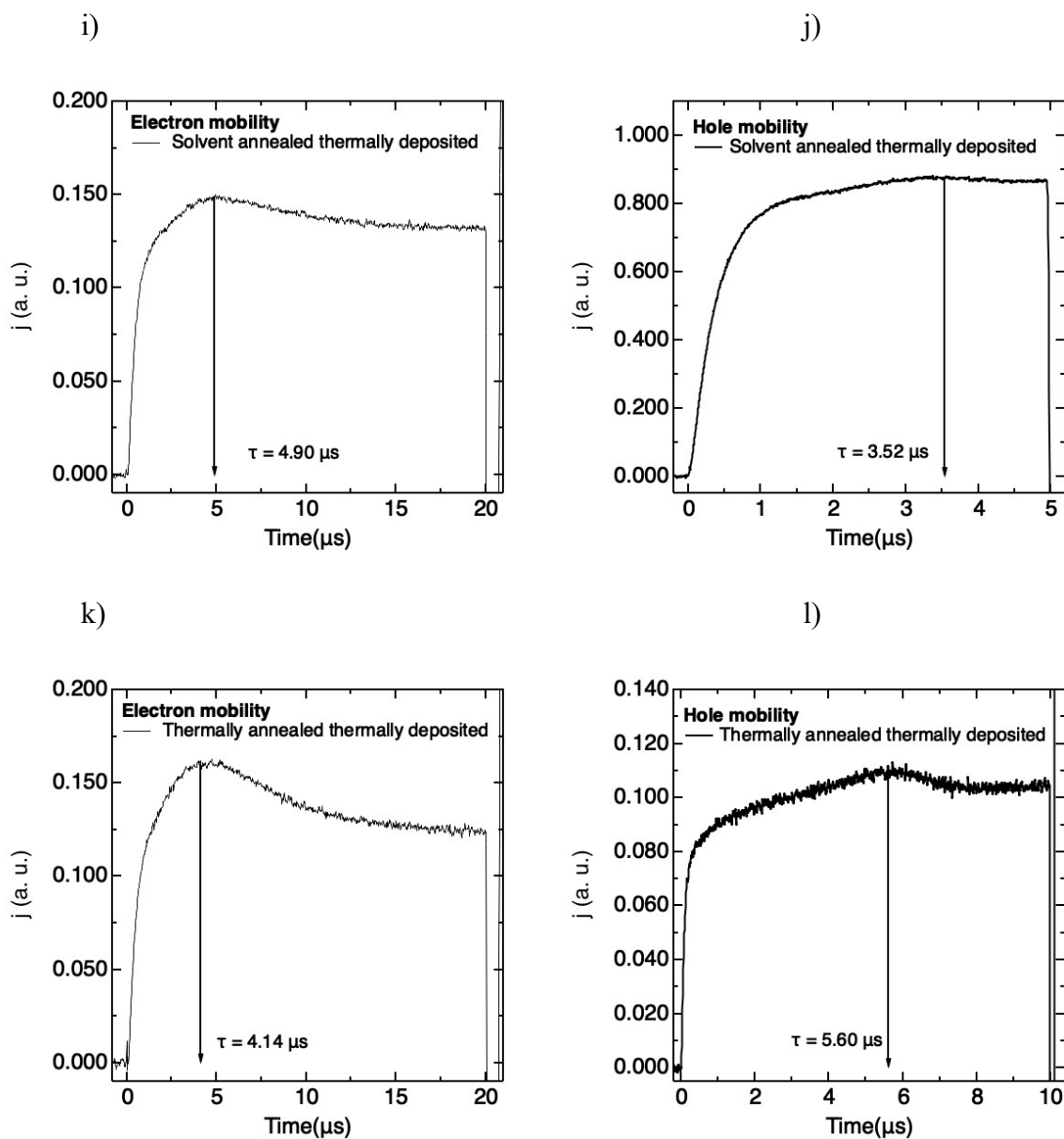

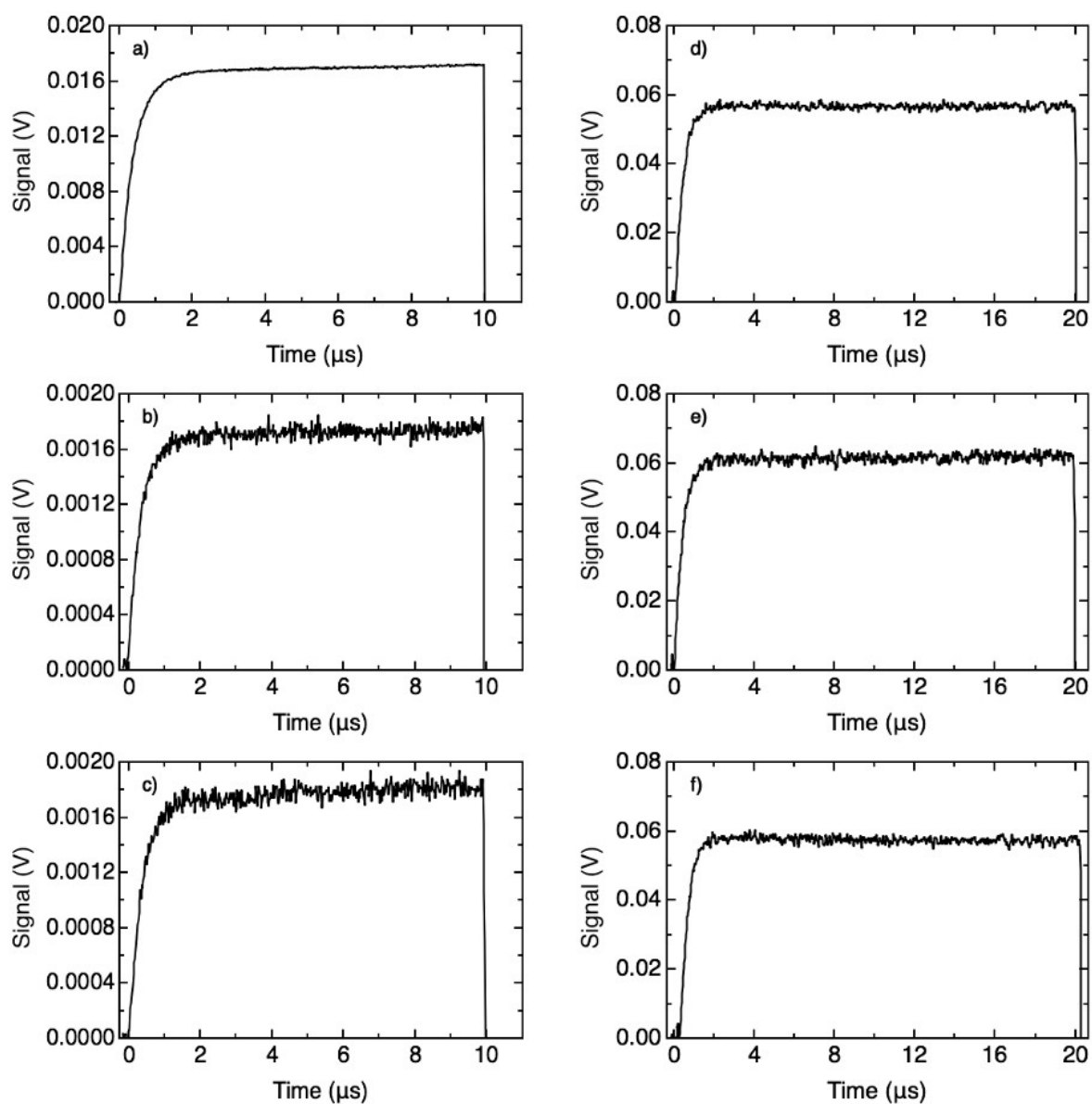c)   d)
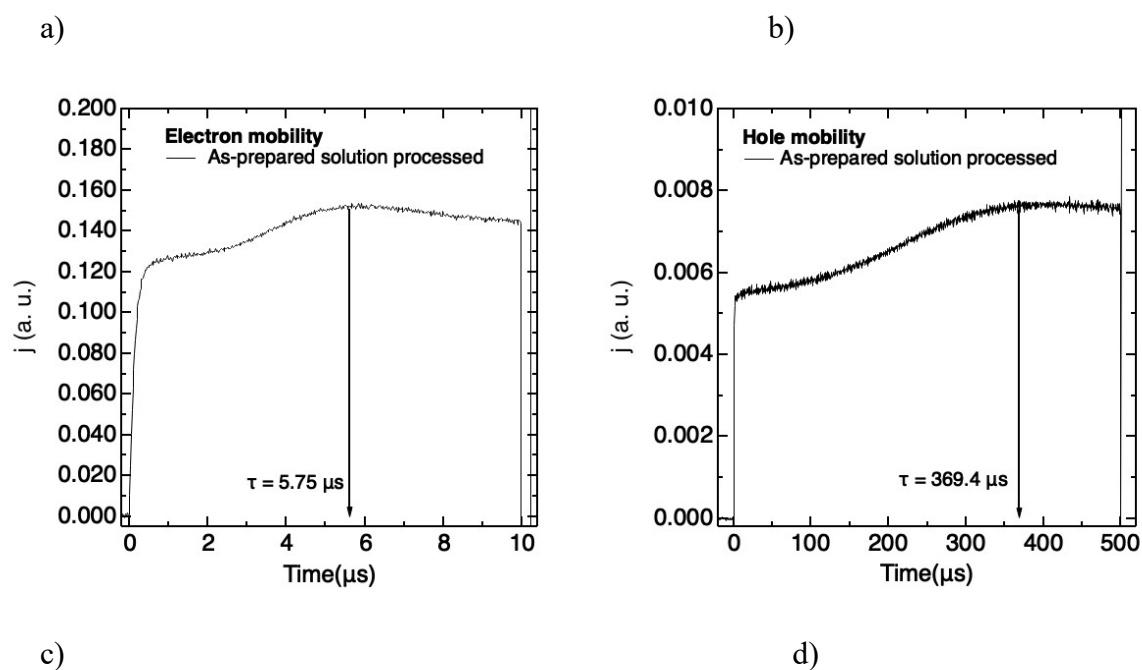
e)

f)

g)

h)
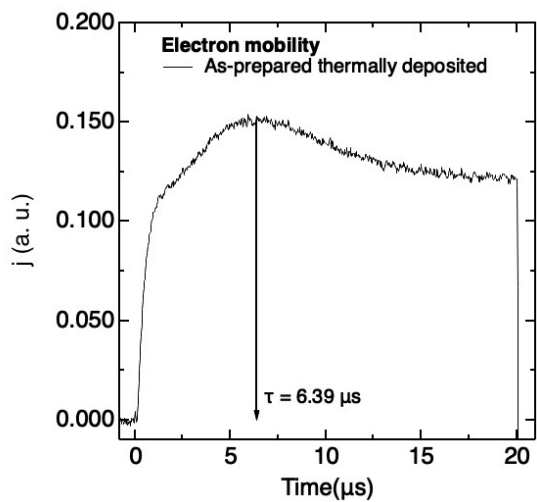
Figure S15. Hole and electron mobilities for solution-processed **D(CPDT-DCV)** films (a–f) and thermally deposited films (g–l) using Metal-Insulator-Semiconductor Charge-Extraction with Linearly-Increasing-Voltage (MIS-CELIV).

Figure S16 Charge-Extraction with Linearly-Increasing-Voltage (CELIV) for calculation of a static dielectric constant ε_{lf} for solution processed **D(CPDT-DCV)** films (a), (b) and (c), and thermally deposited **D(CPDT-DCV)** films (d), (e) and (f).
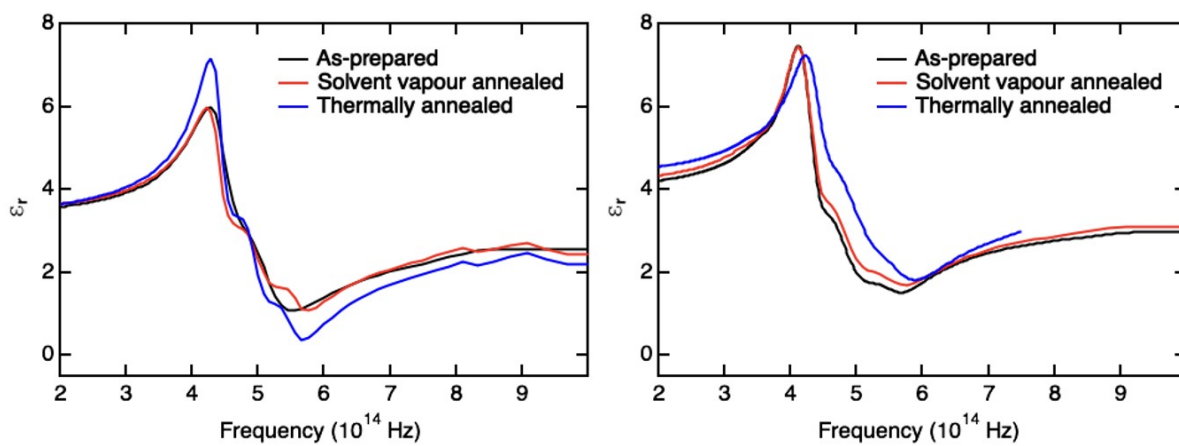
Figure S17 Dielectric constants of the solution-processed **D(CPDT-DCV)** films (left) and the thermally deposited **D(CPDT-DCV)** films (right) *versus* frequency in optical frequency range.
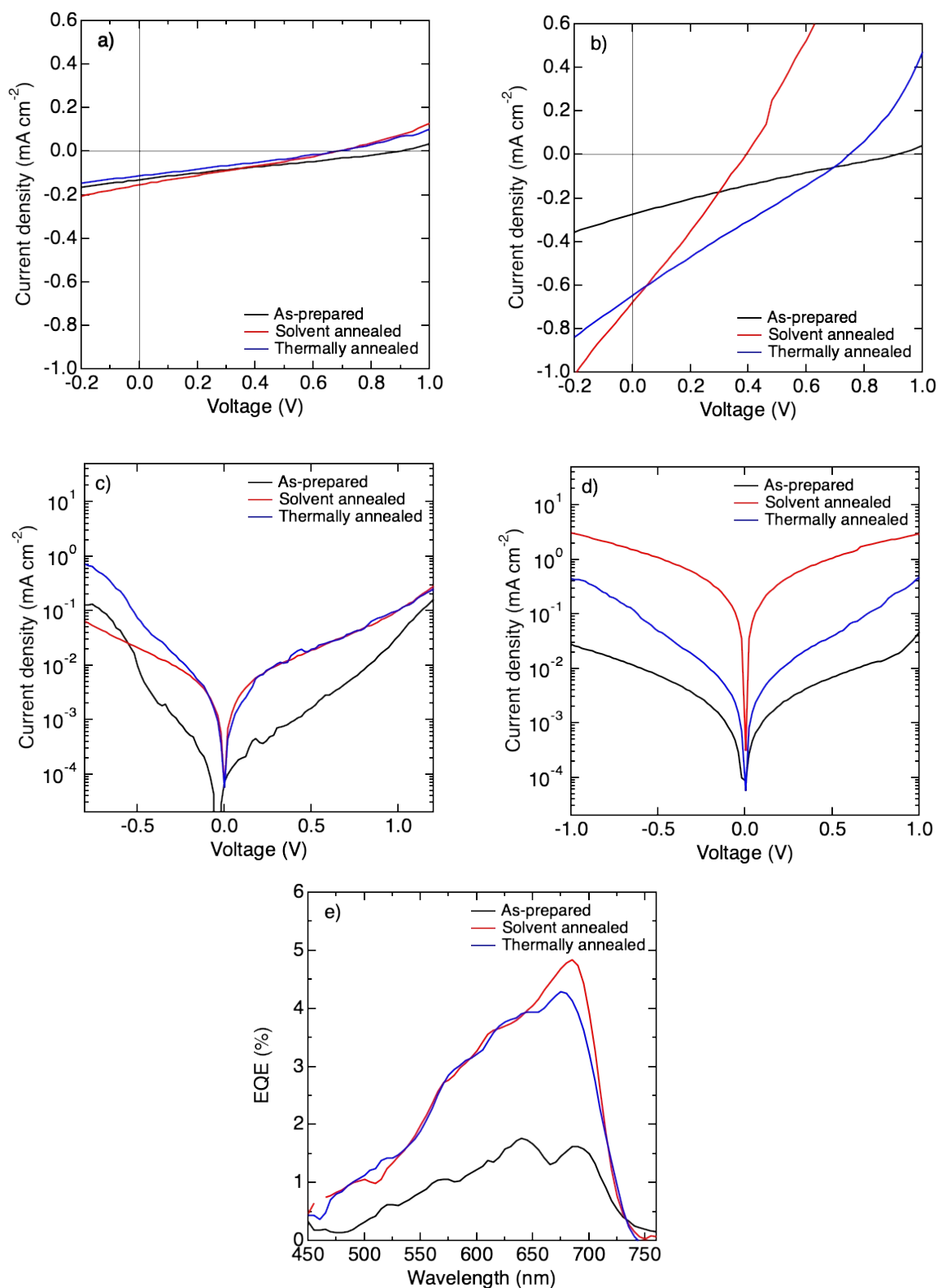
Figure S18. Current density *versus* voltage (*J-V*) characteristics under illumination of 100 mW cm^{-2} of solution-processed (a) and thermally-deposited (b) **D(CPDT-DCV)** with the structure of ITO/PEDOT:PSS/Homojunction (~50 nm)/Ba/Al. Dark current density *versus* voltage (*J-V*) characteristics of solution-processed (c) and thermally-deposited (d) **D(CPDT-DCV)** devices

with the structure of ITO/PEDOT:PSS/Homojunction (~50 nm)/Ba/Al. (e) External quantum efficiency (EQE) of thermally-deposited homojunction devices.

References

1. R. OD, Agilent, CrysAlis PRO, Agilent Technologies Ltd, Yarnton, Oxfordshire, England, 2013.

2. O. V. Dolomanov, L. J. Bourhis, R. J. Gildea, J. A. K. Howard and H. Puschmann, *J. Appl. Cryst.*, 2009, **42**, 339-341.

3. G. M. Sheldrick, *Acta Cryst.*, 2015, **A71**, 3-8.

4. G. M. Sheldrick, *Acta Cryst.*, 2015, **C71**, 3-8.